UNIVERSITY OF CALIFORNIA SAN DIEGO

Optical Resonances for Enhanced Quantum Efficiency Photocathodes

A dissertation submitted in partial satisfaction of the requirements for the degree Doctor of Philosophy

in

Materials Science and Engineering

by

Anna Alexander

Committee in charge:

Prabhakar Bandaru, Chair
Nathan Moody, Co-Chair
Shadi Dayeh
Javier Garay
Zhaowei Liu
Paul Yu

2018

The Dissertation of Anna Alexander is approved, and it is acceptable in quality and form for publication on microfilm and electronically:

Co-chair

Chair

University of California San Diego

2018

Table of Contents

Signature Page 3

Table of Contents 4

Photoemission Theory and Materials 12

Optical and photoemission simulation methods 23

Simulations of plasmonic gratings for photoemission 28

Interference photocathodes 39

References 47

List of Figures

Figure 1: A schematic indicating the parameters used for understanding the influence of surface texture. Engineering the mutual influence of the width: w, height: h, and the period: d, could result in a substantial enhancement of photon absorption and resulting **Error! Bookmark not defined.**

Figure 2: Dependence of the absorption: A (λ=250 nm) for textured Al surfaces as a function of the ridge width (w) and height (h), where peaks in the absorption seem to occur at similar h/w ratios 32

Figure 3: The enhancement of the QE for textured Al surfaces compared with that of planar surfaces as a function of w and h 33

Figure 4: A comparison of the computational simulations (sim: triangles) to the analytical DM (circle) predictions—equation 2 and that of the Dowell model combined with Le Perchec's considerations [47]: equation 19, (DM+P: squares) 33

Figure 5: Dependence of the absorption: A(λ=250 nm) for textured Cu surfaces as a function of the ridge width (w) and height (h) 34

Figure 6: The enhancement of the QE for textured Cu surfaces compared with that of planar surfaces for Copper (λ=250 nm) as a function of the grating geometry (w and h), illustrating dependence of QE on A(λ) 34

Figure 7: A comparison of the computational simulations (sim: triangles) to the analytical DM (circle) predictions—equation 2 and that of the Dowell model combined with Le Perchec's considerations [47]: equation 19, (DM+P: squares) 35

Figure 8: Average QE for aluminum vs the fraction emission from corners. QE is averaged over all 36 simulated Al geometries and put into .1 fraction emission buckets 36

Figure 9: A schematic of a typical photoemission system configuration indicating light incidence (of a specific wavelength: λ) onto a photocathode film deposited on a substrate. The complex refractive index ($n = n + i\kappa$) as well as the dielectric permittivity (ε) and magnetic permeability (μ) of the film and substrate are indicated 40

Figure 10: (a) A plot of the absorption coefficient: A, as a function of photocathode film thickness (h) for various substrates, i.e., Ag: Figure 10(b), W: Figure 10(c), and Al: Figure 10(d), on which the photocathode film is deposited. Also noted on Figure 10(a) is the A calculated assuming an infinitely thick film, *i.e.*, assuming $h = \infty$. 45

List of Tables

Table 1: The refractive index of metals that are typically used as substrates for photocathode films[10][11] 15

Table 2: Optical constants of various commonly used photocathode films: (i) Cs_3Sb[18][19][8], (ii) K_2CsSb[13], [20], (iii) Cs_2Te[21], and (iv) the multi-alkali S20 photocathode[13], [22]. The computed electromagnetic skin depth values at the respective wavelengths 15

Table 3: Constants and components of quantum efficiency for Al and Cu at 250 nm. A(λ) is calculated with equations 3 and 4, Fe-e is calculated using equation 10, η is calculated using equation 8 and Polθ PolΦ is calculated using equations 12-15 with PolΦ assumed to be 1. 31

Acknowledgements

Chapters 1-4, in part, have been submitted for publication of the material as it may appear in A. Alexander, N. A. Moody, and P. R. Bandaru, J. Vac. Sci. Technol. A Vacuum, Surfaces, Film, 2016 and A. Alexander, N. A. Moody, and P. R. Bandaru,, J. Vac. Sci. Technol. B, 2017. The dissertation author was the primary investigator and author of this paper.

Vita

2011 Bachelor of Science, Georgia Institute of Technology

2012 Master of Science, University of California San Diego

2018 Doctor of Philosophy, University of California San Diego

ABSTRACT OF THE DISSERTATION

Optical Resonances for Enhanced Quantum Efficiency Photocathodes

by

Anna Alexander

Doctor of Philosophy

University of California San Diego, 2018

Prabhakar Bandaru, Chair
Nathan Moody, Co-Chair

Photocathodes are devices where electrons are emitted upon illumination by a light source. This dissertation investigates how optical resonances can be used to increase the efficiency of both metal and semiconductor cathodes. We theoretically investigate the use of interferences via surface plasmons created on subwavelength gratings of aluminum photocathodes. Aluminum is used because it can have plasmon resonances at energies above the work function, which gives it a higher efficiency than gold or silver plasmonic cathodes. We predict that plasmonic cathodes could have a ~30x improvement over non-resonant aluminum cathodes and should be substantially more efficient than the currently used Cu cathodes. We also investigate the use of interferences to enhance the efficiency of thin film

semiconductor cathodes. We find that typically used substrates, such as metals (steel, molybdenum, silicon), silicon, or glass, are not expected to show strong interference effects. We find that silver, gold, and aluminum backed photocathodes should show interference effects which could increase the efficiency of cathodes by as much as 30% over bulk photocathodes, and even greater enhancement for thinner cathodes, particularly as compared to current commonly used substrates.

Photoemission Theory and Materials

Motivation

Photocathodes are devices where electrons are emitted upon illumination by a light source. They have many applications, such as optical sensing, high power electronics, and as electron sources [1], [2]. Photocathodes are often used as the electron source for linear accelerators (linacs), due to the stringent requirements of the beam. Photocathodes used in accelerators typically are typically used in very different conditions from most optical devices and have specific requirements that are also uncommon due to how the initial electron emission affects the properties of the electron (or subsequent x-ray, etc.) beam.

Quantum Efficiency

Photocathodes used in accelerator applications are typically evaluated on a combination of properties, which typically describe one of two properties: the intensity of the beam, and the (temporal/spatial/energetic) variation or spread of the beam. The methods in this thesis are largely focused on increasing the intensity of the beam.

Beams in accelerators are typically bunched, and the total bunch charge is an important parameter in accelerator design and applications. The total bunch charge is a function of the electron source and how it is operated, as well as the accelerator design. A more common quality measure for electron sources is the beam current, or quantum efficiency. The beam current is a measure of the current from a photocathode under specific illumination conditions (light wavelength, intensity, pulse structure) and RF conditions (RF field intensity, pulse structure, etc.). The final quality factor related to the intensity of the beam is the quantum efficiency, which is the ratio of emitted electrons to incident photons.

The quantum efficiency is a useful quality parameter because it is a material/device property, rather than a beam property and can thus be easily extended to describe a wide variety of potential operating conditions. However, it cannot be directly used to design and simulate beam properties in an accelerator, and quantum efficiency requirements for a particular application must be back calculated from current and charge requirements. Quantum efficiency is typically measured under low field conditions which assume that the photoemission current, I is linearly proportional to the quantum efficiency and nothing else. Under these conditions, and assuming a CW light source and field, the quantum efficiency can be calculated from the current via equation 1.

$$QE = \frac{Ihc}{P_{in}\lambda} \qquad 1$$

where h is the Planck constant in eV, lambda is the wavelength of the light, c is the speed of light, I is the photoemission current, and Pin is the input power in watts.

Photoemission theory

Photoemission is typically modeled using a 3 step process. The 3 step model, first developed by Spicer, separately models the processes of absorption (electron excitation), electron transport through the material, and transmission/reflection of the electrons at the surface [3]–[5]. The Spicer model has been improved substantially, most notably by Dowell [6], [7] and Jensen [8]. These models, while often using substantial simplifications about properties such as band structure, geometry, surface conditions, etc. are useful both as a basis for more complex simulations and to understand fundamental tradeoffs when optimizing the photoemission process. Below is an example of how such terms are combined [9], slightly modified from Dowell's 2006 paper:

$$QE_{plane} = A(\lambda) \cdot \eta \cdot F_{e-e}(\lambda) \cdot Pol_{\theta} \cdot Pol_{\Phi} \qquad 2$$

A and η describe the absorption process, $F_{e-e}(\lambda)$ describes the electron transport, and Pol_{θ} and Pol_{Φ} describe the emission/reflection at the surface.

Absorption

The absorption is typically related to the reflectivity $R(\lambda)$, through:

$$A(\lambda) = 1 - R(\lambda) \qquad 3$$

where $R(\lambda)$ is the bulk reflectance, which can be calculated analytically using Fresnel's equations.

Assuming normal incidence, this results in equation 4, where n and k are the real and imaginary parts of the refractive index of the metal, and are related to the dielectric constant, $\varepsilon = \varepsilon_r + i\varepsilon_i$ through equations 5 and 6.

$$R = \frac{(n-1)^2 + k^2}{(n+1)^2 + k^2} \qquad 4$$

$$\varepsilon_r = n^2 - k^2 \qquad 5$$

$$\varepsilon_i = nk \qquad 6$$

This assumes that the cathode is infinitely thick. This is typically appropriate for metals. Most metals are highly reflective/absorptive, as can be seen from the optical constants in Table 1. As a result, most metals under illumination in the visible light/low UV (~600nm-250nm) become "infinitely thick" within a few hundred nanometers, which is much thinner than most photocathodes. It may become significant however, if the cathodes are made by sputtering or evaporation onto a different substrate, as evaporated and sputtered films are often very thin, and may become rougher if made very thick.

Table 1: The refractive index of metals that are typically used as substrates for photocathode films[10][11]

Substrate metal	**Refractive index**			
	532nm	405 nm	355 nm	266 nm
Al	0.9 + 6.0i	0.5+4.8i	0.3+4.2i	0.2+3.1i
Ag	0.2 +3.1i	0.1+1.9i	0.2+1.3i	0.8+1.5i
Au	0.5 +2.1i	1.5+1.8i	1.6+1.8i	1.6+1.9i
Cu	0.8 +2.5i	1.3+2.3i	1.2+1.9i	1.5+1.7i
W	3.5 +2.7i	3.2+2.5i	3.2+2.5i	2.8+2.6i

The assumption that the cathode is infinitely thick is less likely to be the case for semiconductor cathodes. Most semiconductor photocathode films in usage are of the order of 10 nm - 50 nm thick[12]–[15][12], [14], [16], [17]. Given the skin depths shown in Table 2, it is likely that most cathodes are not infinitely thick. The implications and consequences of this will be further described in the Interference Photocathodes section.

Table 2: Optical constants of various commonly used photocathode films: (i) Cs_3Sb[18][19][8], (ii) K_2CsSb[13], [20], (iii) Cs_2Te[21], and (iv) the multi-alkali S20

photocathode[13], [22]. The computed electromagnetic skin depth values at the respective wavelengths

Cathode Material	**Refractive index *(skin depth)***			
	λ: 532 nm	λ: 405 nm	λ: 355 nm	λ: 266 nm
Cs_3Sb	3.3 +0.9i *(44 nm)*	2.1+1.7i *(19 nm)*	1.3+1i *(28nm)*	
K_2CsSb	3.2+0.8i *(52 nm)*	2.2+1.2i *(27 nm)*	1.6+1.3i *(21 nm)*	1.3+0.6i *(34 nm)*
Cs_2Te				0.8 +0.8i *(28 nm)*
S20	2.9+0.4i *(106 nm)*	2.8+0.6i *(57 nm)*	2.2+0.2i *(128 nm)*	2.1+0.1i *(163 nm)*

Density of States

The absorption, and spatially resolved absorbed energy distribution determine the location and number of excited electrons. It does not specify the energy or momentum of those electrons. The density of states of a material determines the energy distribution of the excited electrons. This is essentially because according to Fermi's Golden Rule, the probability of an excitation event is proportional to the number of states in each occupied energy level multiplied by the number of states in the unoccupied level that it would transition to. The continuous nature of the density of states results in an energy distribution of excited electrons [5], [18].

Of the total number of excited electrons, only a fraction that have adequate energy to overcome the effective work function (φ_{eff}, after taking into account the Schottky barrier induced lowering[19]) between the metal and the vacuum need to be considered. It is common to assume a flat density of states D(E) to get an expression for QE with an analytical solution. This results in equation 7, given the energy level (E) occupancy of the electrons which is given by the Fermi-Dirac distribution function, $f_{FD}(E)$.

$$\eta = \frac{\int_{E_F+\varphi_{eff}-\hbar\omega}^{\infty} f_{FD}(E)D(E)[1-f_{FD}(E+\hbar\omega)D(E+\hbar\omega)]dE}{\int_{E_F-\hbar\omega}^{\infty} f_{FD}(E)D(E)[1-f_{FD}(E+\hbar\omega)D(E+\hbar\omega)]dE} \qquad 7$$

The limits correspond to electrons being excited from at/near the Fermi energy (E_F) with allowance for the energy provided by the incoming photons (of energy $\hbar\omega$). Equation 7 reduces to equation 8 if D(E) is constant between the limits of integration.

$$\eta = (\hbar\omega - \phi_{eff})/\hbar\omega \qquad 8$$

This assumption is a good first order approximation for metals, for which the square root dependence of the DOS may be approximated as constant at high enough energies. This model is too simplistic for semiconductors but can be easily modified to effectively model semiconductors by replacing the constant DOS with a DOS derived from a basic band model.

In general, the bandgap present in semiconductors can increase QE by reducing the fraction of optical transitions which result in excited electrons with an energy below the vacuum level. The lack of states in the bandgap can also prevent certain types of scattering events, such as electron-electron scattering, also increasing QE. This effect becomes stronger as Eg/Ea becomes higher [4], [20], [21].

More complex photoemission models have been derived which explicitly use the band structures of materials and quantum models of absorption to determine the optical transitions and excited electron distribution[22], [23]. These models are substantially more complex than 3 step models, which could make them more accurate, as well as potentially making predictions without any experimental data required.

Electron Transport

The photons penetrate the material to an average distance corresponding to the electromagnetic skin-depth (l_s). The excited electrons are isotropically excited at a depth "r" below the surface. A fraction of these electrons move toward the metal-vacuum interface, during which a further proportion is lost to scattering by electron-electron scattering (with an energy dependent mean free path: $\lambda_{e\text{-}e}(E)$), and/or electron-phonon scattering. For electrons excited in metals, electron-electron scattering is dominant, and electron-photon scattering can be ignored. The fraction of electrons that do survive and reach the surface may be taken to be proportional to r and is given by:

$$f(r,E,\lambda,\alpha)=\frac{1}{\lambda_{opt}}e^{-r\left({}^{1}/_{\lambda_{opt}(\lambda)}+{}^{1}/_{\lambda_{e-e}(E)\cos(\alpha)}\right)} \qquad 9$$

The α indicates the angle made by the electron mean free path in the metal with the surface normal and $\lambda_{e-e}(E)\cos(\alpha)$ indicates the distance between the point at which the electron is excited and the nearest surface. It has been indicated that one can reasonably put $\lambda_{e-e}(E)\cos(\alpha)$ as a constant: $F_{e\text{-}e}$. Such an assumption ignores the angular and energy dependence of the scattering and is equivalent to assuming a relatively constant mean free path. A justification was the minimal influence on the net *QE*. Consequently, the net probability of an electron reaching the surface without scattering, normalized by the expected photon penetration length (λ_{opt}, the intensity skin depth defined in equation 11: $F_{e\text{-}e}$ (λ), which modulates the net *QE* is given by:

$$\begin{aligned} F_{e-e}(\lambda) &= \int_0^\infty f(r,\lambda)dr \\ &= \int_0^\infty \frac{1}{\lambda_{opt}} e^{-r\left({}^{1}/_{\lambda_{opt}(\lambda)}+{}^{1}/_{\lambda_{e-e}(E)\cos(\alpha)}\right)}dr \\ &= \frac{1}{1+\frac{\lambda_{opt}}{\lambda_{e-e}}} \end{aligned} \tag{10}$$

$$\lambda_{opt} = \lambda/4\pi k \tag{11}$$

For semiconductors, a similar approach can be taken as a first approximation. Instead of considering $\lambda_{e\text{-}e}$ to be an electron scattering length, it can instead be considered to be a more general escape length. This is more appropriate for semiconductors, for which multiple types of scattering may be significant [8], [24]. In addition, the energy lost per scattering event is typically substantially lower than that of electron-electron scattering. As a result, electrons in semiconductors can often be scattered multiple times before being emitted, increasing both the quantum efficiency and the response time [4], [16], [25]–[30].

The assumption that scattering occurs isotropically is somewhat challenging, as many authors have claimed that most electron scattering events are not isotropic [18], [31]–[33]. More accurately modelling this from a physics perspective is challenging however, both due to the dependence of many scattering mechanisms on band structure and crystal orientation, as well as a general lack of data on elastic scattering events, which may be more likely to be isotropic. As a result, assuming isotropic behavior is a reasonable first approximation.

Electron transmission at the surface

The probability of electron emission from the assumes a barrier that exists only in the direction perpendicular to the surface. As a result, only the perpendicular component of the energy/momentum is evaluated when determining whether the excited electrons have sufficient energy. Further, the 3 step model assumes complete electron emission/transmission for energies greater than the barrier, and complete reflection for those with energy less than the barrier. Reflected electrons are ignored in most metal models, because the dominance of electron-electron scattering means that any scattering event would reduce the energy of the electron too much for subsequent electron emission to be possible, even if the electron trajectory was perfectly normal to the surface.

Only a fraction of the angular distribution of excited electrons of the total possible angular range will be emitted (which is $0 < \theta < \pi$, for the polar coordinate, and $0 < \Phi < 2\pi$, for the azimuthal counterpart). For a flat surface, the polar and azimuthal components can be considered independently. The polar fraction of emitted electrons would be the ratio of those with sufficient angular momentum perpendicular to the surfaced divided by the total angular momentum range. The emitted electrons are considered through an integral of the following form[6]:

$$Pol \quad = \int_0^{cos^{-1}(\sqrt{\frac{E_F+\varphi_{eff}}{E+\hbar\omega}})} \sin(\theta)\, d\theta \tag{12}$$

Such a value of θ_{max} is in accord with the emission of electrons perpendicular to the surface,

$$\sqrt{2m(E+\hbar\omega)}\cos(\theta) \geq \sqrt{2m(E_F+\varphi_{eff})} \tag{13}$$

If the electrons were emitted over all the possible angles, then:

$$Pol_{\theta max} = \int_0^{\pi} \sin(\theta)\, d\theta \tag{14}$$

The ratio of 12/14 would then give the emission efficiency with respect to the polar emission of electrons, as:

$$Pol_{\theta} = Pol/Pol_{\theta max} \tag{15}$$

The azimuthal electron emission probability, *i.e.*, Pol_{F} is assumed to be unity.

The net *QE* of an un-textured/plane surface, QE_{plane}, is equal to the product of the expressions listed in Equations 3,7,10, and 15, and is given by equation 2.

<u>Metals vs semiconductors</u>

Both metals and semiconductors are commonly used as cathode materials. While many of the tradeoffs can be determined through a comparison via the 3 step model, there are some important differences between typically used metals and typically used semiconductors which cannot be derived solely from this analysis. Specifically, most semiconductors used for photoemission are alkali antimonides, or similar photocathodes. Specifically, they are compound semiconductors, with at least one alkali constituent, which is most commonly cesium. Examples include Cs_3Sb, K_2CsSb, Cs_2Te, CsI, and Na_2KSb.

The use of alkali metals, particularly cesium results in a reduced work function which increases the QE. However, alkali metals are also highly reactive. As a result, these cathodes can must be made and operated under very high vacuum, and still have very short lifetimes, on the order of tens of hours. Reproducibility and thermal stability are also challenges. In addition, most semiconductor photocathodes are thin films in usage are of the order of 10 nm - 50 nm thick[12]–[15][12], [14], [16], [17], with larger thickness being used for higher absorption due to presumed reduced influence of grain boundaries, without much quantitative rationale[16].

Historically, stainless steel, tungsten and various glasses were common substrate materials[15], [34]–[36] . Silicon has recently become a very popular substrate material due to its low surface roughness. Some metal substrates, in particular Cu, cannot be easily used as substrates, particularly using the older sequential evaporation technique, as the Cu alloys with Sb, preventing formation of a semiconductor cathode[37], [38] .

Metal cathodes typically used include most metals typically used in accelerator fabrication, such as tungsten, stainless steel, copper, niobium, lead, and molybdenum. They are typically polished, and cleaned, but no additional special treatments are typically applied. As a result, they are fairly stable, and are considered to have an nearly infinite lifetime, though aging and degradation does occur over a time period of months-years [1].

Optical and photoemission simulation methods

Optical simulations

Finite element EM simulations were used, specifically the RF module of COMSOL® Multiphysics to determine the excited electron distribution. The RF module of Comsol solves a wave equation, which is needed to get accurate excited electron spatial profiles both in nanostructures and thin film photocathodes. Light enters and exits the simulation through a port boundary condition at the top, which permits the calculation of S parameters, as well as reflection and transmission. Infinite boundary conditions are applied on the sidewalls, which simulates an infinite array of nanostructures, or an infinitely large thin film. These boundary conditions are appropriate for cathodes, which typically have an area of mm^2 to cm^2, much larger than a unit cell. The bottom boundary condition is typically perfect electric conductor boundary condition, i.e. $E=0$. This is accurate so long as the fields have sufficiently decayed before reaching the boundary. This can be validated by confirming that the reflection, and absorbed energy are not changed if the thickness of the substrate is changed.

Fields from the electron gun (both DC and RF) are modeled as DC fields on a perfect conductor. This is for several reasons. First, since the frequency of most RF guns is a few GHz, the wavelength of any RF field is on the order of tens of centimeters [1], [39]–[44]. Given that the size scales of the nanostructures are on the order of nanometers, and the photoemission process occurs over femtoseconds to picoseconds, the entire nanostructure sees uniform fields in time and space, making a DC approximation valid. Further, during simulation validation of metals using structures with analytical solutions such as spheres and plates of finite thickness, we found that solutions using perfect conductor boundary conditions resulted in more accurate solutions, likely because it eliminated error from simulating the fields inside the metal.

Grating simulations have rounded corners with a radius of curvature of 1 nm. Applying a rounded corner does not substantially affect the absorption/reflection. It does substantially change the field profile near the surface and is required to get a surface field intensity that is independent of mesh density. Rounding the corners is a common way to achieve this, and 1 nm is the most common radius of curvature [2], [45].

Photoemission simulations

The photoemission simulations used are in-house developed MATLAB® code, derived from Dowell's 3 step model [46] . The same mesh is used for the photoemission simulations and the Comsol EM simulations. As a result, the mesh is nonuniform with varying mesh sizes and density, with higher densities near the surface and near geometric features. With regard to mesh limitations, it must be ensured that (a) the mesh size be smaller than ~ 0.1 λ_{laser}, to accurately resolve the EM fields, and (b) that the mesh density for the EM/optical simulations be at least as dense as the PE mesh, to minimize sensitivity. We found that a maximum mesh size in the vicinity of 0.5 nm was sufficient to result in flat QE sensitivity of less than 10%. The absorbed energy distribution was obtained through the absorbed power per volume from the EM simulations.

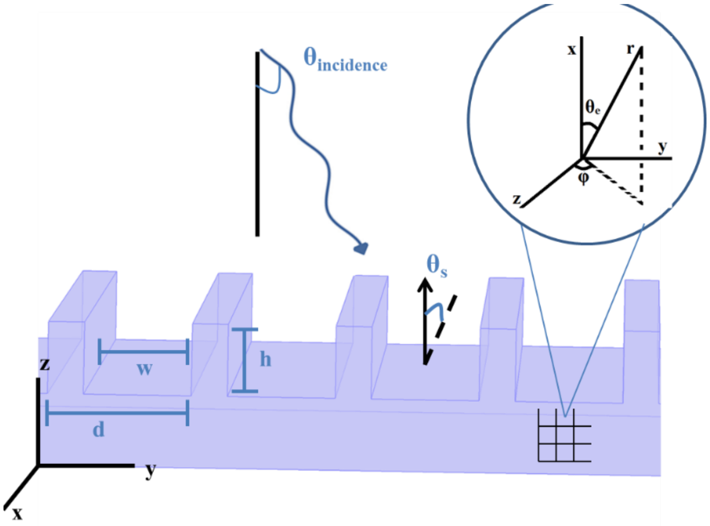

Figure 1: A schematic indicating the parameters used for understanding the influence of surface texture. Engineering the mutual influence of the width: *w*, height: *h*, and the period: *d*, could result in a substantial enhancement of photon absorption and resulting *QE*.

Modifications to the 3 step model

We modified the equations 2-15, stated for the *QE* of a flat surface, to be correct for nonuniform surfaces applied at the level of a unit mesh element. Taking the case of equation 2, the macroscale absorbance $A(\lambda)$ was replaced by the absorbed power *per* unit mesh element, normalized to the input power, $P_{in.}$ The $f(r,E,\lambda,\alpha)$ - see equation 9, which considers the fraction of photo-excited electrons below the surface, *per* unit optical skin depth is a measure of the absorption as well (note that the form of *f* is that of the Lambert-Beer law). The consequent probability of that an electron reach the surface without scattering is modified to:

$$F_{e-e}(\lambda) = \sum_{\Phi=0}^{\Phi=2\pi} \sum_{\theta_e=0}^{\theta_e=\pi} \sum_{r=0}^{r=\infty} e^{-r(\theta_e,\Phi)\left[1/\lambda_{e-e}\right]} \qquad 16$$

Here, the *exp* (*-r/λ_{e-e}*) is considered at the individual element level through emission over the entire range of θ and Φ. The electron scattering angle *within* the element is written as θ_e and maybe distinct from the θ_s – the polar angle of emission (from equation 12**)** for non-flat surfaces. Such a modification also enables estimation of electron emission from multiple surfaces. A similar summation over θ_s and Φ was done to calculate Pol_q and Pol_{F} at the individual element level. The volume of the mesh element serves as a normalizing factor for the modified *QE* estimation.

The final consequence of the 2D structure is that the terms are no longer independent, and that each mathematical operation must be applied before summing in θ, Φ, x, y, z. So, while flat models can be written in the form of equation 8, where each term is independent and has a known, integratable form

$$QE = \eta \int_{y0}^{y1} \mathrm{dA}(\lambda)\mathrm{dy} \int_{y0}^{y1} d(\mathrm{F}_{\mathrm{e-e}})\mathrm{dy} \int_{\theta 0}^{\theta 1} \mathrm{d}(\mathrm{Pol}_{\theta})\, \mathrm{d}\theta \int_{\boldsymbol{\Phi 0}}^{\boldsymbol{\Phi 1}} \mathrm{d}(\mathrm{Pol}_{\Phi})\mathrm{d}\Phi \qquad 17$$

our model has the form in equation 18. The integrals have been replaced by sums, as discussed above, because we are no longer guaranteed known, integratable expressions for each term for an arbitrary geometry. Similarly, equations 2 and 17 assume that a given y value will always result in the same distance from the surface, and that given θ, Φ values will always result in the same angle with respect to the surface. This allows each term to be considered independently but is clearly not always the case for a structured surface. Thus, equation 18 mimics the behavior of a discretized group of electrons by applying each of the steps in the model before summing.

$$QE = \eta \sum\nolimits_{x,y,z} \sum\nolimits_{\theta} \sum_{\Phi} dA * dF_{e-e} * d\,Pol_{\theta} * dPol_{\Phi} \qquad 18$$

This means that strictly speaking, there is no one value that can accurately describe the contribution of Pol_{θ}, Pol_{Φ}, A(λ) or $F_{e\text{-}e}$ to the overall photoemission behavior, since the terms are interdependent.

Simulations of plasmonic gratings for photoemission

We consider incident photon illumination with an energy that is larger than that of the work function of the metal. Typically, the values of the work function (φ) are not precisely known and vary strongly with the surface condition and crystal orientation. We considered, photons of wavelength (λ = 250 nm, with energy ~ 4.96 eV) incident on two metals, *i.e.*, Al (with φ =4.1 eV) and Cu (with φ=4.3 eV).

Mechanisms for Plasmon Enhanced Photoemission

Strong absorption of light in a planar two-dimensional grating with grooves that are strongly sub-wavelength (almost by two orders of magnitude) in height (h) and width (w), has been considered [47]. These structures are interesting for several reasons.

First is that the enhanced absorption and surface fields. The enhanced surface fields are interesting both from an electron acceleration perspective, but also because sufficiently intense surface fields could also reduce φ_{eff}, providing an additional source of QE enhancement. Both enhanced absorption and surface fields are common features of plasmon resonances. However, plasmonic gratings with dimensions on the order of the wavelength of light, such as the typical grating coupling, have a very strong angular dependence on the absorption/reflection. Resonances typically occur at relatively high angles, 40-70°. Both the sharpness of the resonance with respect to angle and the high angles required may be challenging for use in accelerator applications, which typically use angles near normal incidence (~10°) and may have limited abilities to tune or specify the incidence angle. This is because cathodes are typically inside an RF cavity with few and small windows, and due to limited space as a result of additional diagnostic equipment, etc. needed for accelerator functioning.

With these subwavelength gratings, the increased absorption was ascribed to the excitation of a resonance condition, coupled to surface plasmon polaritons (SPPs) in the electrostatic regime, where the plasmons are not allowed to penetrate significantly into the material, *i.e.*, to less than that of the usual optical skin depth. The analytical solution for the modified skin depth: λ_{mod}, was derived to be:

$$\lambda_{mod} = \lambda_{opt}\sqrt{\frac{\varepsilon}{\varepsilon - 1}}\left[-\Gamma + \sqrt{\Gamma^2 + 1}\right], \Gamma = \frac{\lambda_{opt}}{2w\sqrt{\varepsilon(\varepsilon - 1)}} \qquad 19$$

A lowered skin depth (λ_{mod}) of the SPPs would result in greater excitation efficiency but is not directly correlated higher absorption. The derivation of equation 19 for the λ_{mod} was based on the exact eigenfunction solution for square wave gratings[48], assuming that the period, *d* of the grating was very large, that w was small enough for the SPPs on each side to interact, and a normal laser angle of incidence. Moreover, it was also assumed that the imaginary part (ε_i) of the dielectric constant (ε) was much smaller compared to the real part (ε_r). This is true for aluminum, which has a dielectric constant at 250 nm, $\varepsilon_{Al} = -8 + i$ [49]

However, such assumptions may not always be realistic for practical application. r Cu in Eqn. (6b). For example, the dielectric constant of Cu with an incident laser illumination at 250 nm is $\varepsilon_{Cu} = -0.75 + 5.25\,i$ [49].

Consequently, while analytical relations may be derived under specific approximations, the understanding of the response of realistic textured surfaces requires extensive EM simulations. It is unclear whether this model will be qualitatively accurate for

Cu given this limitation. Such considerations are in view of the complex inter-relationships between the number and the nature of the electron emitting surfaces, as well as the concomitant EM field interactions. The resultant three-dimensional field interactions may influence each of the terms in equation 2, and hence the *QE* as well.

Another attribute of surface texture that could substantially contribute is the presence of electron emitting surfaces, a feature that is conspicuously absent in flat surfaces. Enhanced electric fields at the corners may also aid in the electron emission. However, such effects may also be quenched, *e.g.*, in a square grating where electron emission may just be between the two sidewalls. Indeed, it was found in the simulations that more than one emitting surface was necessary for energy conservation.

Estimates of Upper limits of Plasmon Enhanced Photoemission

While likely quantitatively inaccurate, equations 2-17 can be used to determine potential areas of improvement and derive maximum values for the QE enhancement. Table 3 gives analytical values of $A(\lambda)$, F_{e-e}, Pol_{θ} Pol_{Φ}, η for flat Al and Cu using equation 4 assuming a laser wavelength of 250 nm. Rough estimates for the maximum QE possible for a grating for Al and Cu at 250 nm can be derived assuming the following: η is unchanged by the grating, the maximum value for $A(\lambda)$ and F_{e-e} is 1. Since the grating ridges have 3 flat sides, the maximum enhancement of Pol_{θ} Pol_{Φ} is 3. This results in a maximum normalized QE of 113 for Al and 13.5 for Cu.

Table 3: Constants and components of quantum efficiency for Al and Cu at 250 nm. A(λ) is calculated with equations 3 and 4, Fe-e is calculated using equation 10, η is calculated using equation 8 and Polθ PolΦ is calculated using equations 12-15 with PolΦ assumed to be 1.

Property	**Flat Al**	**Flat Cu**
E_F	11.7 [50]	7 [50]
Work function	4.1 [51]	4.31[6]
λ_{e-e}	4 nm [52], [53]	5.5 nm [6]
A(λ)	.074	.66
F_{e-e}	.36	.33
H	.1734	.1309
Pol_θ Pol_Φ	.00131	.00138
QE	6e-05	7.28 e-4

Optical and Photoemission Simulation Results

While Al is a more ideal plasmonic material, Cu is much more commonly used. This is likely due to its higher QE, which is largely a result of its higher A, which is .64 at 250 nm compared to .07 for Al. Many of the other parameters are similar for both the metals, *e.g.*, (i) the λ_{e-e} for Al is 6 nm[52], [53], while the λ_{e-e} for Cu is 4 nm, and (ii) the Fermi energy[50] (E_F) for Al is 11.7 eV, while the E_F for Cu is 7 eV.

Thus, while Al is a better modeling prototype, similar simulations could also have practical applications understanding the effects of nonperfect surfaces of currently used cathodes. Figure 2 shows the absorbance spectra of 36 Al gratings, with the characteristic resonant peaks. Figure 3 plots the normalized quantum efficiency in the same configuration, showing that the absorption enhancement is the dominant enhancement mechanism for Al, given the nearly identical profiles. The peak locations are in the locations predicted by Le Perchec and occur at the fixed h/w ratio where the vertical sidewall plasmons couple with a Fabry-Perot resonance. Figure 4 confirms the linear dependence of QE on absorption and shows the predicted QE by using A(λ) in Dowell's model, as well as using A(λ) and λ_{mod} in Dowell's model. Doing this accurately reproduces the features of the curve, but underpredicts QE due to the inability of the surface model to incorporate interaction and multisurface affects.

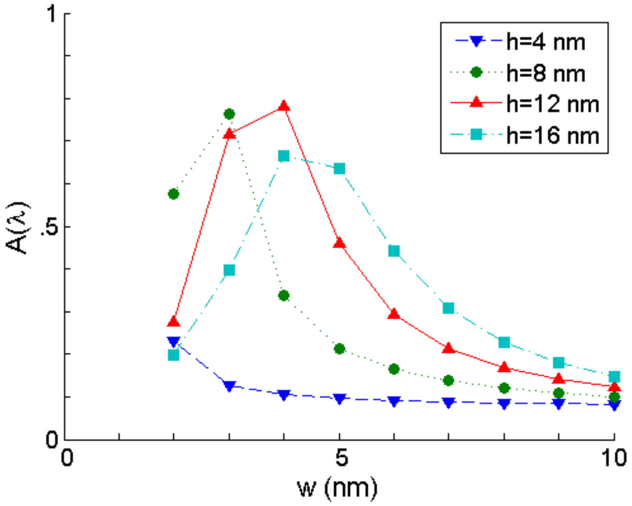

Figure 1: Dependence of the absorption: A (λ=250 nm) for textured Al surfaces as a function of the ridge width (w) and height (h), where peaks in the absorption seem to occur at similar h/w ratios

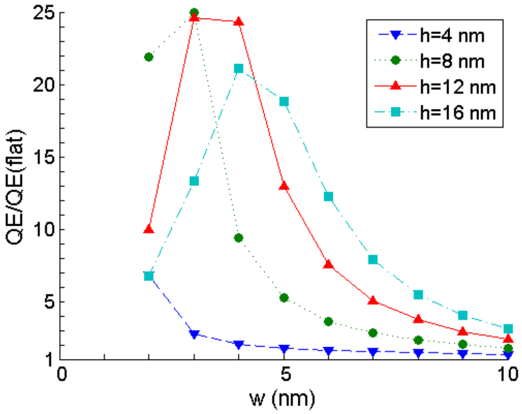

Figure 2: The enhancement of the QE for textured Al surfaces compared with that of planar surfaces as a function of w and h

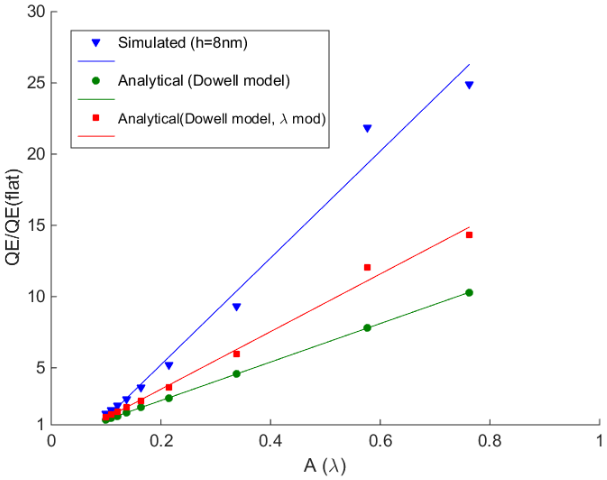

Figure 3: A comparison of the computational simulations (sim: triangles) to the analytical DM (circle) predictions—equation 2 and that of the Dowell model combined with Le Perchec's considerations [47]: equation 19, (DM+P: squares)

Similar, less dramatic curves are possible for Cu. Figures 5 and 6 shows the absorption profile and QE profile of Cu, confirming again that absorption is the dominant QE enhancement mechanism. Figure 7 shows that given a real A and w values, the flat model can reproduce the features of the simulated curve, but this time overpredicts the QE.

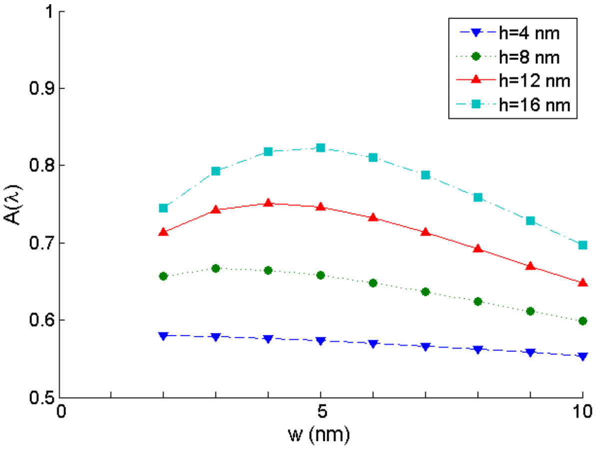

Figure 4: Dependence of the absorption: A(λ=250 nm) for textured Cu surfaces as a function of the ridge width (w) and height (h)

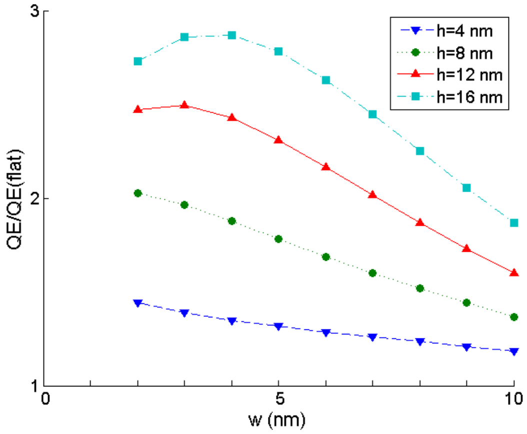

Figure 5: The enhancement of the QE for textured Cu surfaces compared with that of planar surfaces for Copper (λ=250 nm) as a function of the grating geometry (w and h), illustrating dependence of QE on A(λ)

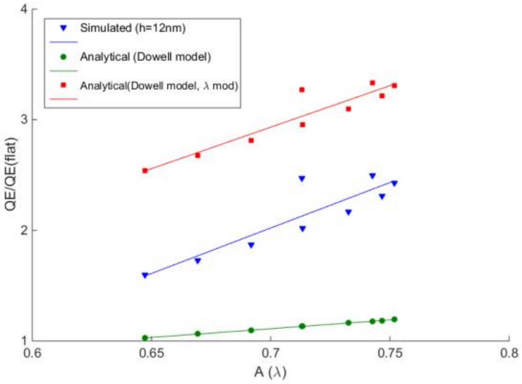

Figure 6: A comparison of the computational simulations (sim: triangles) to the analytical DM (circle) predictions—equation 2 and that of the Dowell model combined with Le Perchec's considerations [47]: equation 19, (DM+P: squares)

One plausible question is the degree to which these trends above are created due to the effects of the corners, rather than surface plasmons. In both Cu and Al, increased QE is correlated with a decreased fraction of total photoemission coming from the corners. Higher photoemission and lower photoemission from corners are associated with regimes where the SPP-Fabry Perot resonance is present. This is partially because as h decreases, the relative volume near corners increases. In addition, most of the Fabry-Perot resonances are expected to occur at relatively high h values. Thus, this is in line with expectations. The fact that the fraction of emission from corners increases substantially as the geometric parameters shift away from this resonance is a good check and indicates that the increased QE is not solely due to enhanced absorption in the corners, which could occur without a plasmon resonance. The differences between the behavior of Al and Cu also gives insight on how material properties can change the overall sensitivity to corners. Overall, the field distributions, and photoemission of Cu are less sensitive to the geometry than Al. For an identical geometry, the photoemission of Cu tends to have a lower fraction coming from the corners. It also has a much lower absorption enhancement and a larger fraction of photoemission from the top and bottom of the gratings, which are not affected by the Fabry Perot-SPP resonance. Thus, Cu is less affected both by the corners, and the resonance which, when active, mitigates the affects of the corners.

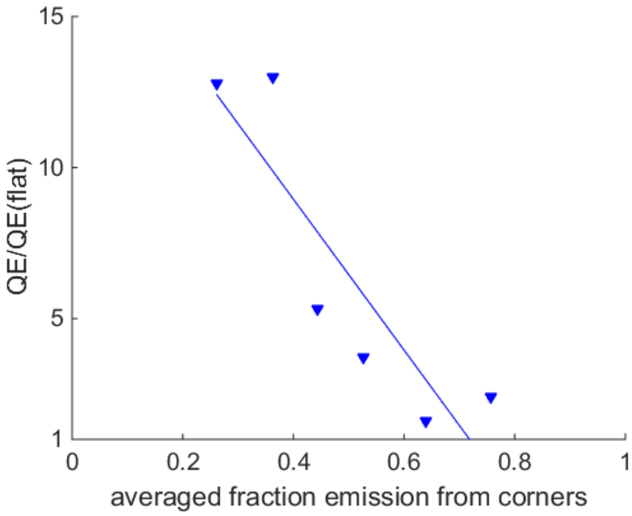

Figure 7: Average QE for aluminum vs the fraction emission from corners. QE is averaged over all 36 simulated Al geometries and put into .1 fraction emission buckets

Further, while the simulations attest to the complexity of predicting QE behavior, they also give insight into general guidelines for optimizing metal structures for increased QE. First, since absorption will likely dominate the enhancement, only structures that have shown high absorption in EM models should be considered. Second, subwavelength gratings with dimensions on the order of the electric field skin depth should have higher photoemission than larger gratings.

This is due to 2 reasons. The first is that this is the regime in which electrostatic plasmons are possible, resulting in a reduced $\lambda_{e\text{-}e}$ and increased $F_{e\text{-}e}$. The second is that these dimensions are small enough for some electrons on the ridges of the gratings to emit to multiple surfaces, increasing $Pol_\theta\ Pol_\Phi$. Since both effects occur at the same size regime, it is difficult to separate the affects, particularly given the interaction term. However, at gratings with dimensions much larger than the electric skin depth ($2\lambda_{opt}$), both affects disappear. The effect on $\lambda_{e\text{-}e}$ disappears due to the requirement for small w (<15 nm for Al, <40 for Cu) and the requirement that d be subwavelength but larger than the field skin depth. The enhancement to $Pol_\theta\ Pol_\Phi$ decreases because as the dimensions of the grating increase, the electrons from a given differential volume element become more and more likely to scatter before they see multiple surfaces, and the grating surface appears more as a series of flat surfaces at different angles than as 3 variably accessible surfaces.

The enhancement due to the subwavelength structure is confirmed by the simulations. For the geometries above, the maximum QE enhancement that could be attributed to absorption alone is 10.5 for Al and 1.3 for Cu, given a maximum $A(\lambda)$ in the current simulations of ~.75 and .85 for Al and Cu respectively. However, Al shows a maximum enhancement of ~24 and Cu shows a maximum enhancement of 2.9. Thus, the subwavelength gratings improved the QE beyond by a factor of ~2.3 for Al and Cu.

Subwavelength gratings, with dimensions on the order of the electric field skin depth substantially improve the QE of Al and Cu. This is due to plasmonic resonances; in the low power limit, corners are unimportant. Even for complex structures, the terms are largely independent; Given these findings, it would be intriguing to further investigate the behavior of small structures with a large number of surface angles, such as spherical nanoparticles. Small, round nanoparticles could enhance QE by increasing the fraction of total electrons with sufficient momentum perpendicular to the surface through having a large range of surface angles. Further, round shapes have additional potential in more realistic power regimes where nonuniform surface fields could increase emittance substantially. However, the plasmon behavior of gratings and nanoparticles is quite distinct, so it is difficult to extend these results to nanoparticles without extensive additional simulations.

Interference photocathodes

Enhanced light absorption arises through carefully matching the impedance of the photocathode-substrate system to that of the vacuum to which electrons are emitted. We have observed, that absorption could be increased by an order of magnitude through proper design. Moreover, we find that the often-used Lambert-Beer (L-B) law may not be a reliable indicator of the extent of absorption in many configurations. This work focuses on reflection mode photocathodes, and not on transmission mode devices, as the former is most commonly used in accelerator applications.

Given that flat photocathode surfaces are typically preferred: Figure 9, as rough surfaces increase emittance[1], it is posited that minimizing reflections at the various interfaces (*i.e.,* vacuum-photocathode film, film-substrate) would be beneficial for enhanced photon absorption. In this context, one may consider typical anti-reflecting film characteristics commonly used in optical applications through the deployment of selective destructive interference[54]. However, the photon absorption processes, (a) for the conversion of photons to excite electrons in the photocathode film, and (b) in the substrate/metal, due to the imaginary component of the refractive index, imply the need for different design principles.

Through a careful review of previous work[55]–[57], we hypothesized that the reflection of energy from the substrate and re-deposition into the photocathode - along with reducing transmission through the substrate, could be beneficial. In this paper, we predict quantitatively the specific criteria through which such benefits could be harnessed through modeling characteristics of a typical low electron affinity K_2CsSb photocathode film[58], at an incident wavelength of 532 nm.

Analytical absorption models of a three layer (thin film) system

In describing the photon absorption processes in a photocathode film of thickness: *h*, for facilitating subsequent photoemission into the vacuum (*V*), the net absorption coefficient: *A* would be related to the detailed absorption profile - *a*(*x*) through the thickness of the film (*x*) – see Figure 9 for axes orientation- by:

$$A = \int_0^h a(x)dx \tag{20}$$

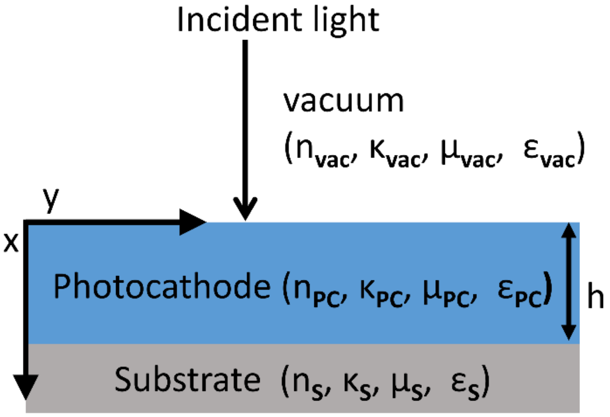

Figure 8: A schematic of a typical photoemission system configuration indicating light incidence (of a specific wavelength: λ) onto a photocathode film deposited on a substrate. The complex refractive index ($\tilde{n} = n + i\kappa$) as well as the dielectric permittivity (ε) and magnetic permeability (μ) of the film and substrate are indicated

The materials (*photocathode: PC*, and substrate: *S*) are each described through a respective complex refractive index: $\tilde{n} = n + i\kappa$. Considering normal incidence of the photons (*e.g.*, through laser illumination from vacuum): Figure 9, the reflection coefficients at the vacuum-photocathode film interface (*i.e.*, $r_{V\text{-}PC}$) and the photocathode film – substrate interface (*i.e.*, $r_{PC\text{-}S}$) are the Fresnel coefficients[59], *i.e.*,

$$r_{V-PC} = \frac{\tilde{n}_V \ - \tilde{n}_{PC}}{\tilde{n}_V + \tilde{n}_{PC}} \qquad 21$$

$$r_{PC-S} = \frac{\tilde{n}_{PC} \ - \tilde{n}_S}{\tilde{n}_{PC} + \tilde{n}_S} \qquad 22$$

The electric field in the photocathode film is:

$$E_y = \ E_o e^{i\omega t}(1 + r_{V-PC})e^{i\tilde{n}_{PC}kx} \qquad 23$$

The magnetic field (H_z) could then be derived, from: $H = (-1/\mu) \int \nabla \ X \ E \ dt$, to be:

$$H_z = \ -\left(\frac{E_o}{\omega\mu_o\mu_{PC}}\right)\tilde{n}_{PC} k e^{i\omega t}(1 + r_{V-PC})e^{i\tilde{n}_{PC}kx} \qquad 24$$

While the net power density flow into the material could be parameterized through the Poynting vector in the complex form[60]; (S_x) = ½ $E_y \cdot H_z^*$ where H_z^* is the complex conjugate of H_z, we define a *differential* power density (P_a) to describe the power absorption through the thickness of the material, as: $P_a = \nabla \cdot Re(S_x)$, as:

$$P_a = -\left(\frac{\kappa_{PC} \ k^2 \ \tilde{n}_{PC}}{\omega\mu_o\mu_{PC}}\right)|E_o(1 + r_{V-PC})|^2 e^{-x/\lambda_{opt}} \qquad 25$$

where $\lambda_{opt} = 1/(2k\kappa_{PC})$ and is related to a *characteristic* decay length of the P_a. The input power (P_{in}), at x =0, is:

$$P_{in} = -\left(\frac{k\tilde{n}_{vac}}{2\omega\mu_o\mu_V}\right)|E_o|^2 \tag{26}$$

The absorption profile, $a(x) = P_a / P_{in}$, would be:

$$a(x) = -\left(\frac{2\kappa_{PC}\, k\tilde{n}_{PC}}{\mu_o\mu_{PC}}\right)|(1 + r_{V-PC})|^2 e^{-{x}/{\lambda_{opt}}} \tag{27}$$

Equation 27 may be alternately written in accord with the well-known L-B relation:

$$a(x) = I_o e^{-{x}/{\lambda_{opt}}},\ \ I_o = -\left(\frac{2\kappa_{PC}\, k\tilde{n}_{PC}}{\mu_o\mu_{PC}}\right)|E_o(1 + r_{V-PC})|^2 \tag{28}$$

However, such derivations do not particularly consider back-reflections and interactions of the waves in the *PC* film. For a finite film thickness of *h*, considering the forward and backward waves yields an alternate relation for the electric field, as:

$$E_x = E_o e^{i\omega t}(c_f e^{i\tilde{n}_{PC}kx} + c_b e^{-i\tilde{n}_{PC}kx}) \tag{29}$$

Here, $c_f \left(= \frac{(1+r_{V-PC})}{1-r_{V-PC}r_{PC-S}e^{2i\tilde{n}_2kh}}\right)$ and $c_b\left(= c_f\, r_{PC-S}e^{2i\tilde{n}_2kh}\right)$denote the amplitude of the contributions from the *forward* and *backward* traveling waves, respectively. Consequently, considering the differential power density through the Poynting relationship, *etc.*, we derive a modified absorption profile of the form:

$$a(x) = I_o^f \left|e^{-{x}/{2\lambda_{opt}}} + r_{PC-S}e^{2i\tilde{n}_{PC}kh}e^{{x}/{2\lambda_{opt}}}\right|^2 \tag{30}$$

$$I_o^f = \left(\frac{(1 + r_{V-PC})}{1 - r_{V-PC}r_{PC-S}e^{2i\tilde{n}_2kh}}\right)^2 \left(\frac{-k\kappa_{PC}}{2\omega\mu_o\mu_{PC}}\right) \tag{31}$$

It can be observed that equation 30 reduces to the form of equation 28 when $\tilde{n}_2$ is purely imaginary and $\tilde{n}_2kh \gg 1$. In this case c_b approaches zero with the implication that the backward traveling wave does not influence the electric field in the *PC* film. Essentially, this is equivalent to assuming an infinitely thick film and it is evident that the L-B relation implicitly incorporates such an assumption. As we have previously discussed that *PC* films have thickness of the order of 10-50 nm– due to constraints related to the electromagnetic skin depth as well as the electron escape depth (see Table 2 for optical constants related to typically used films), we posit that the Lambert-Beer relation is not accurate and instead, forms such as equation 30 need to be deployed for assessing the absorption profiles of *PC* films. Consequently, many extant theoretical models of photoemission[4], [12], [14], [16] may need to be modified. The second term in equation 30 is most indicative of finite film thickness effects, and at a (h/λ_{opt}) ratio close to unity, there would be substantial reflected wave amplitude which may influence the a (x), and photoemission.

Results of interference simulations

We plot the absorption coefficient: *A*, computed from incorporating equation 30 in equation 20 for various substrates (with varying r_{PC-S}) in Figure 10(a). Several aspects related to such graphs are to be noted, *e.g.*, an *A* maximum (i) occurs at a specific thickness, *i.e.*, at h_{max}, into the film and *not* at the surface, as would be expected from the L-B relation, (ii) is sensitive to the particular substrate, *i.e.*, Ag: Figure 10(b), W: Figure 10(c), and Al: Figure 10(d), on which the *PC* film is deposited. Specifically, the h_{max} is ~ 28nm (for Al substrate), ~ 20 nm (for Ag and Cu substrates), ~ 18 nm (for Au substrate), and ~ 42 nm (for W substrate). Also noted in Figure 10(a) is the *A* calculated assuming an infinitely thick film, *i.e.*, with $h = \infty$, as the upper limit to the integral in equation 10. Moreover, *PC* films of similar *A* have differing a (x) profiles and consequently, the thickness corresponding to the maximum in $a(x)$ is different from h_{max}. For example, deploying a K_2CsSb film on a Ag substrate results in a h_{max} of ~ 20 nm, while $a(x)$ is largest for h ~ 14 nm. Generally, for $h < h_{max}$, the maximum in $a(x)$ is at the surface while for $h > h_{max}$, the maximum is *in* the film. A plausible reason is that the A is enhanced when the forward and the reflected waves are π radians out of phase at the vacuum side of the *V-PC* interface. Changing the substrate (see Table 3 for the optical constants of the various metal substrates typically used in photoemission studies) influences the specific thickness at which maxima in A and $a(x)$ occur due to the variation of r_{PC-S}. Generally, a high substrate reflectivity would enhance interference effects in the *PC* film and contribute to enhanced absorption.

It is pertinent to consider, from Figures 10(b) – (d), that $a(x)$ variation is much more involved compared to what would expected from the L-B relation which specifies an exponential drop in the absorption from the surface through the film thickness. The latter aspect could be rationalized through the neglect of backwards traveling waves. While the $a(x)$ magnitude seems to be larger than that estimated from the L-B relation for certain specific values of h (typically less than h_{max}), the overall A is nevertheless smaller due to the smaller upper limit of the integral in equation 10. Alternately, for $h > h_{max}$, the L-B solution generally overestimates $a(x)$.

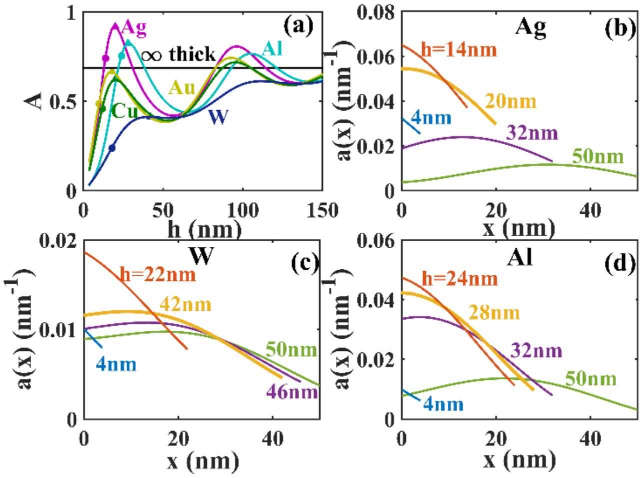

Figure 9: (a) A plot of the absorption coefficient: A, as a function of photocathode film thickness (h) for various substrates, i.e., Ag: Figure 10(b), W: Figure 10(c), and Al: Figure 10(d), on which the photocathode film is deposited. Also noted on Figure 10(a) is the *A* calculated assuming an infinitely thick film, *i.e.*, assuming $h = \infty$.

We will now extend such insights into *a* (*x*) variation to the respective influences on the *QE* of photoemission. In a basic model, while the incident photons penetrate the *PC* film – substrate system to an average distance corresponding to the electromagnetic skin-depth (~λ_{opt}), only the electrons excited at a depth equivalent to λ_{esc} are eligible to drift to the *PC*-vacuum interface. A larger λ_{esc} implies a greater likelihood of the electrons escaping from the photocathode and an increased F_e. However, as previously discussed equation 30 is more valid and was applied for assessing the probability (F_e) of a photo-excited electron reaching the surface, through:

$$F_e = \int_0^h a(x) e^{-x/\lambda_{esc}}\, dx \qquad 32$$

It is then indicated clearly through equation 32 that, for a given a (x), electrons excited closer to the surface (smaller x) would have a greater probability of photoemission. The evaluation of F_e hinges on the knowing λ_{esc}, which is not a well-characterized quantity. While more accurately known for metals (*e.g.*, the λ_{esc} has been reported[7], [9], [61] as ~ 4 nm for Al and ~ 5.5 nm for Cu at an incident wavelength of 250 nm), for semiconductor photocathodes, the λ_{esc} is larger[16], [55] and in the range of 20 nm – 40 nm.

While this analysis has been used to optimize the cathode QE, it could also be used to reduce QE variability, with respect to roughness and thickness. This is important since photocathodes are rarely atomically flat. It is also useful because most cathodes are thin films, and thus it is useful to be estimate at what thickness the cathode can reasonably be expected to be infinitely thick. Generally, for $\lambda_{opt} << \lambda_{esc}$, the only requirement is that the wave be sufficiently decayed such that any interference effects do not change the A, implying a film thickness, h of the order of $5\lambda_{opt}$. When $\lambda_{opt} > \lambda_{esc}$, the shape of the $a(x)$ curve matters, but only for depths shallow enough that the electrons can actually be emitted. The relevant thickness can be derived through using equation (10) and yields h ~ $5\lambda_{opt}$.

In summary, we have proposed that electron emission from photocathode thin films could be significantly enhanced – by as much as a factor of three through a comprehensive consideration of the influence of film substrates and interference effects in the films. The influence of the finite thickness of the films as well as the complex refractive indices of the film and the substrate plays a major role in obtaining such enhancement.

References

[1] D. H. Dowell *et al.*, “Cathode R&D for future light sources,” *Nucl. Instruments Methods Phys. Res. Sect. A Accel. Spectrometers, Detect. Assoc. Equip.*, vol. 622, no. 3, pp. 685–697, Oct. 2010.

[2] E. Forati, T. J. Dill, A. R. Tao, and D. Sievenpiper, “Photoemission-based microelectronic devices,” *Nat. Commun.*, vol. 7, no. May, pp. 1–8, 2016.

[3] J. G. Endriz and W. E. Spicer, “Study of Aluminum Films. II. Photoemission Studies of Surface-Plasmon Oscillations on Controlled-Roughness Films,” *Phys. Rev. B*, vol. 4, no. 12, pp. 4159–4184, Dec. 1971.

[4] W. E. Spicer and A. Herrera-Gomez, “Modern theory and applications of photocathodes,” *Proc. SPIE*, vol. 2022, no. International Symposium on Optics, Imaging and Instrumentation, pp. 18–35, 1993.

[5] C. N. Berglund and W. E. Spicer, “Photoemission Studies of Copper and Silver: Theory,” *Phys. Rev.*, vol. 136, no. 4A, pp. 4–16, 1964.

[6] D. H. Dowell and J. F. Schmerge, “Quantum efficiency and thermal emittance of metal photocathodes,” *Phys. Rev. Spec. Top. - Accel. Beams*, vol. 12, no. 7, p. 074201, Jul. 2009.

[7] D. H. Dowell, F. K. King, R. E. Kirby, and J. F. Schmerge, “In situ cleaning of metal cathodes using a hydrogen ion beam,” *Phys. Rev. Spec. Top. - Accel. Beams*, vol. 9, no. 6, p. 063502, Jun. 2006.

[8] K. L. Jensen, B. L. Jensen, E. J. Montgomery, D. W. Feldman, P. G. O’Shea, and N. A. Moody, “Theory of photoemission from cesium antimonide using an alpha-semiconductor model,” *J. Appl. Phys.*, vol. 104, no. 4, p. 044907, Aug. 2008.

[9] A. Alexander, N. A. Moody, and P. R. Bandaru, “Enhanced quantum efficiency of photoelectron emission, through surface textured metal electrodes,” *J. Vac. Sci. Technol. A Vacuum, Surfaces, Film.*, vol. 34, no. 2, p. 021401, Mar. 2016.

[10] “Radiation from Apertures and Beam Waves,” in *Electromagnetic Wave Propagation, Radiation, and Scattering*, Hoboken, NJ, USA: John Wiley & Sons, Inc., 2017, pp. 169–200.

[11] A. D. Rakić, A. B. Djurišić, J. M. Elazar, and M. L. Majewski, “Optical properties of metallic films for vertical-cavity optoelectronic devices,” *Appl. Opt.*, vol. 37, no. 22, p. 5271, Aug. 1998.

[12] K. L. Jensen, P. G. O’Shea, and D. W. Feldman, “Generalized electron emission model for field, thermal, and photoemission,” *Appl. Phys. Lett.*, vol. 81, no. 20, p. 3867, Nov. 2002.

[13] S.W. Harmer, R. Downey, Y. Wang, and P.D. Townsend, “Variation in optical constants between photocathodes,” *Nucl. Instruments Methods Phys. Res. A,* vol. 564, pp. 439–450, 2006.

[14] K. L. Jensen, N. A. Moody, D. W. Feldman, E. J. Montgomery, P. G. O’Shea, and P. G. O’Shea, “Photoemission from metals and cesiated surfaces,” *J. Appl. Phys.*, vol. 102, no. 7, pp. 0–19, Oct. 2007.

[15] L. Cultrera *et al.*, "Growth and characterization of rugged sodium potassium antimonide photocathodes for high brilliance photoinjector," *Appl. Phys. Lett.*, vol. 103, no. 10, 2013.

[16] P. D. Townsend *et al.*, "Designs for waveguide and structured photocathodes with high quantum efficiency," *J. Phys. D. Appl. Phys.*, vol. 39, no. 8, pp. 1525–1536, Apr. 2006.

[17] L. Cultrera, C. Gulliford, A. Bartnik, H. Lee, and I. Bazarov, "Ultra low emittance electron beams from multi-alkali antimonide photocathode operated with infrared light," *Appl. Phys. Lett.*, vol. 108, no. 13, 2016.

[18] K. F. Brennan, *The Physics of Semiconductors*. Cambridge: Cambridge University Press, 1999.

[19] R. S. Muller, T. I. Kamins, and M. Chan, *Device electronics for integrated circuits*, 3rd ed. New York: John Wiley and Sons, 2003.

[20] T. Rao and D. H. Dowell, *An Engineering Guide To Photoinjectors*. 2014.

[21] K. L. Jensen *et al.*, "A photoemission moments model using density functional and transfer matrix methods applied to coating layers on surfaces: Theory," *J. Appl. Phys.*, vol. 123, no. 4, p. 045301, Jan. 2018.

[22] P. Zhang and Y. Y. Lau, "Ultrafast strong-field photoelectron emission from biased metal surfaces: exact solution to time-dependent Schrödinger Equation," *Sci. Rep.*, vol. 6, no. 1, p. 19894, Apr. 2016.

[23] S. Karkare, W. Wan, J. Feng, T. C. Chiang, and H. A. Padmore, “One-step model of photoemission from single-crystal surfaces,” *Phys. Rev. B*, vol. 95, no. 7, p. 075439, Feb. 2017.

[24] R. F. Pierret, “Advanced Semiconductor Fundamentals,” *Book*, vol. 121, no. 7, p. 221, 1987.

[25] M. Niigaki, T. Hirohata, T. Mochizuki, S. Uchiyama, H. Kan, and T. Hiruma, “Electron diffusion length and escape probabilities for cesiated and hydrogenated polycrystalline diamond photocathodes,” *Appl. Phys. Lett.*, vol. 75, no. 22, p. 3533, Nov. 1999.

[26] P. D. Townsend, “Photocathodes—past performance and future potential,” *Contemp. Phys.*, vol. 44, no. 1, pp. 17–34, Jan. 2003.

[27] W. Greschat, H. Heinrich, and P. Römer, “Quantum Yield of Cs3Sb Photocathodes as a Function of Thickness and Angle of Incidence,” *Adv. Electron. Electron Phys.*, vol. 40, pp. 397–408, 1976.

[28] S. H. Kong, J. Kinross-wright, D. C. Nguyen, and R. L. Sheffield, “Cesium telluride photocathodes,” *J. Appl. Phys.*, vol. 77, no. 11, p. 6031, 1995.

[29] D. G. Fisher, “Sources of photoemission in Na 3 Sb thin films Sources of photoemission in Na 3 Sb thin films*,” *J. Appl. Phys.*, vol. 47, no. 3471, 1976.

[30] R. A. Loch, “Cesium-Telluride and Magnesium for high quality photocathodes,” 2003.

[31] F. Jona, “Preparation and properties of clean surfaces of aluminum,” *J. Phys. Chem. Solids*, vol. 28, no. 11, pp. 2155–2160, Nov. 1967.

[32] X. Liu, R. Stock, and W. Rudolph, “Ballistic electron transport in Au films,” *Phys. Rev. B*, vol. 72, no. 19, p. 195431, Nov. 2005.

[33] K. Seeger, *Semiconductor physics*. 2004.

[34] A. di Bona *et al.*, “Development, operation and analysis of bialkali antimonide photocathodes for high-brightness photo-injectors,” *Nucl. Instruments Methods Phys. Res. Sect. A Accel. Spectrometers, Detect. Assoc. Equip.*, vol. 385, no. 3, pp. 385–390, Feb. 1997.

[35] T. Vecchione, J. Feng, W. Wan, and H. Padmore, “HIGH QE, LOW EMITTANCE, GREEN SENSITIVE FEL PHOTOCATHODES USING K2CSSB,” *Proc. FEL2011*, pp. 179–182, 2011.

[36] M. Bastaninejad *et al.*, “Evaluation of niobium as candidate electrode material for dc high voltage photoelectron guns,” *Phys. Rev. Spec. Top. - Accel. Beams*, vol. 15, no. 8, pp. 1–11, 2012.

[37] T. Vecchione *et al.*, “A low emittance and high efficiency visible light photocathode for high brightness accelerator-based X-ray light sources,” *Appl. Phys. Lett.*, vol. 99, no. 3, p. 034103, Jul. 2011.

[38] J. Smedley *et al.*, “HIGH EFFICIENCY VISIBLE PHOTOCATHODE DEVELOPMENT.”

[39] B. L. Rickman, J. A. Berger, A. W. Nicholls, and W. A. Schroeder, “Intrinsic electron beam emittance from metal photocathodes: The effect of the electron effective mass,” *Phys. Rev. Lett.*, vol. 111, no. 23, pp. 1–5, 2013.

[40] M. C. Divall *et al.*, “Intrinsic emittance reduction of copper cathodes by laser wavelength tuning in an rf photoinjector,” *Phys. Rev. Spec. Top. - Accel. Beams*, vol. 18, no. 3, pp. 1–6, 2015.

[41] W. S. Graves, F. X. Kärtner, D. E. Moncton, and P. Piot, “Intense Superradiant X Rays from a Compact Source Using a Nanocathode Array and Emittance Exchange,” *Phys. Rev. Lett.*, vol. 108, no. 26, p. 263904, Jun. 2012.

[42] E. Prat, S. Bettoni, H. H. Braun, R. Ganter, and T. Schietinger, “Measurements of copper and cesium telluride cathodes in a radio-frequency photoinjector,” *Phys. Rev. Spec. Top. - Accel. Beams*, vol. 18, no. 4, pp. 1–7, 2015.

[43] A. Lorusso, F. Gontad, L. Solombrino, E. Chiadroni, E. Broitman, and A. Perrone, “Tight comparison of Mg and Y thin film photocathodes obtained by the pulsed laser deposition technique,” *Nucl. Instruments Methods Phys. Res. Sect. A Accel. Spectrometers, Detect. Assoc. Equip.*, vol. 836, pp. 57–60, 2016.

[44] E. Sabia, G. Dattoli, A. Dipace, and G. Messina, “Free-electron laser triggered photocathodes,” *Phys. Plasmas*, vol. 15, no. 3, 2008.

[45] G. Toscano *et al.*, “Surface-enhanced Raman spectroscopy: nonlocal limitations,” *Opt. Lett.*, vol. 37, no. 13, p. 2538, Jun. 2012.

[46] K. L. Jensen, P. G. O’Shea, and D. W. Feldman, “Emittance of a photocathode: Effects of temperature and field,” *Phys. Rev. Spec. Top. - Accel. Beams*, vol. 13, no. 8, p. 080704, Aug. 2010.

[47] J. Le Perchec, P. Quémerais, a. Barbara, and T. López-Ríos, “Why Metallic Surfaces with Grooves a Few Nanometers Deep and Wide May Strongly Absorb Visible Light,” *Phys. Rev. Lett.*, vol. 100, no. 6, p. 066408, Feb. 2008.

[48] P. Sheng, R. Stepleman, and P. Sanda, “Exact eigenfunctions for square-wave gratings: Application to diffraction and surface-plasmon calculations,” *Phys. Rev. B*, vol. 26, no. 6, pp. 2907–2916, Sep. 1982.

[49] H.-J. Hagemann, W. Gudat, and C. Kunz, “Optical constants from the far infrared to the x-ray region: Mg, Al, Cu, Ag, Au, Bi, C, and Al_2O_3,” *J. Opt. Soc. Am.*, vol. 65, no. 6, p. 742, Jun. 1975.

[50] N. W. Ashcroft and N. D. Mermin, *Solid State Physics*. Orlando, FL: Saunders College, 1976.

[51] W. M. Haynes, *CRC Handbook of Chemistry and Physics, 95th Edition*, 95th ed. CRC Press, 2014.

[52] M. Bauer, S. Pawlik, and M. Aeschlimann, “Electron dynamics of aluminum investigated by means of time-resolved photoemission,” in *Optoelectronics and High-Power Lasers & Applications*, 1998, pp. 201–210.

[53] J. Quinn, “Range of Excited Electrons in Metals,” *Phys. Rev.*, vol. 126, no. 4, pp. 1453–1457, May 1962.

[54] G. R. Fowles, *Introduction to Modern Optics*, 2nd ed. New York, NY: Dover Publications, 1975.

[55] J. A. Love and J. R. Sizelove, “Interference-Enhanced Photoemission,” *Appl. Opt.*, vol. 7, no. 1, pp. 11–16, 1968.

[56] E. G. Ramberg, “Optical factors in the photoemission of thin films.,” *Appl. Opt.*, vol. 6, no. 12, pp. 2163–70, Dec. 1967.

[57] M. A. Novice and J. Vine, “Optical means for enhancing the sensitivity of a tri-alkali photocathode.,” *Appl. Opt.*, vol. 6, no. 7, pp. 1171–8, Jul. 1967.

[58] D. Motta and S. Schönert, “Optical properties of bialkali photocathodes,” *Nucl. Instruments Methods Phys. Res. Sect. A Accel. Spectrometers, Detect. Assoc. Equip.*, vol. 539, no. 1–2, pp. 217–235, 2005.

[59] W. Chang, *Principles of Optics for Engineers*. Cambridge, MA: Cambridge University Press, 2015.

[60] J. D. Jackson, *Classical Electrodynamics*. New York: John Wiley, 1999.

[61] D. R. Lide, *CRC Handbook Chemistry and Physics*, 85th ed. BocaRaton, FL, 2004.